ACS APPLIED MATERIALS & INTERFACES

www.acsami.org

Research Article

Using N–I–N Photodiodes Made of Perovskite Single Crystals for Low Noise Gamma-Ray Spectroscopy

Xin Wang,* Yubing Xu, Yuzhu Pan, Shunjie Chai, Jie Wu, Jingda Zhao, Yuwei Li, Zhiwei Zhao, Qing Li, Jun Wu, Jing Chen, Byung Seong Bae, Jianming Zhou, Ying Zhu, Wei Lei,* and Xiaobao Xu*

Cite This: *ACS Appl. Mater. Interfaces* 2024, 16, 12106–12114

Read Online

ACCESS | Metrics & More | Article Recommendations | Supporting Information

ABSTRACT: Solution-processed lead halide perovskite single crystals (LHPSCs) are believed to have great potential in gamma-ray spectroscopy. However, obtaining low-defect LHPSCs from a solution at low temperatures is difficult compared to obtaining Bridgman single crystals such as CdTe and Si. Herein, noise from the intrinsic defects of LHPSCs is considered as the main problem hindering their gamma-ray detection performance. By isolating the defect-induced holes in LHPSCs via energy barriers, we show that NIN photodiodes based on three types of LHPSCs, i.e., $MAPbBr_3$ (MA = CH_3NH_3), $MAPbBr_{2.5}Cl_{0.5}$, and cascade LHPSCs, have demonstrated good energy resolution in the range of 6.7–10.3% for 662 keV ^{137}Cs gamma-ray photons. The noise for >10 mm^3 devices is low, in the order of 340–860 electrons, and the electron collection efficiency reaches 23–43%. These results pave the way for obtaining low-cost, large, high energy-resolution gamma-ray detectors at room temperature (300 K).

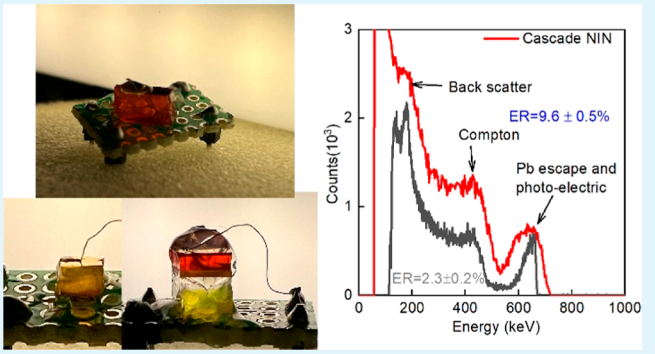

KEYWORDS: *NIN photodiode, low noise, gamma-ray spectroscopy, perovskite single crystals, epitaxial growth*

Downloaded via Byung Seong Bae on March 31, 2024 at 14:09:34 (UTC).
See https://pubs.acs.org/sharingguidelines for options on how to legitimately share published articles.

INTRODUCTION

Gamma-ray detection has been widely used in nuclear monitoring, medical inspection, and scientific research.[1,2] Semiconductors containing elements with a high atomic number that have a large mobility–lifetime product and high resistivity can detect gamma-ray photons at room temperature.[3,4] Generally, high-purity semiconductors, including expensive CdTe and CdZnTe single crystals, have been applied in gamma-ray detectors.[5−10]

Recently, lead halide perovskite single crystals (LHPSCs) $MAPbX_3$ (MA = CH_3NH_3) have been considered as the next-generation room-temperature semiconductors for gamma-ray detection.[11−14] Owing to the high atomic number of Pb, Br, and I, LHPSCs could have a large absorption coefficient for hard gamma-ray photons. Their unique soft lattice structure makes them highly defect tolerant.[15] Additionally, the large mobility–lifetime product of 10^{-2}–10^{-3} cm^2 V^{-1} endows LHPSCs with a satisfactory charge collection efficiency under bias.[16−18] Especially, LHPSCs could be grown from a solution using low-cost, low-purity raw materials.[19,20] Consequently, increasing attention has been paid to LHPSC-based gamma-ray detectors.

The defects and slow response speed prevent solution-processed $MAPbX_3$ single crystals from achieving high performance in gamma-ray spectroscopy. The high level of noise in LHPSCs under high external bias is a serious problem. The noise includes the injection charges from electrodes under bias. Further, the defects inside the LHPSCs would randomly release charges under bias, which are large enough to obscure the single gamma-ray signal of ∼10 fC. For example, an $MAPbBr_3$ LHPSC is very easy to grow, with a large crystal size and cubic shape, which should make it one of the best choices for gamma-ray detection.[13,14,21] However, the intrinsic defects in $MAPbBr_3$ LHPSC-based gamma-ray detectors have prevented them from resolving 662 keV gamma-ray photons in many previous studies.[1,14] Additionally, the response speed of thick, LHPSC-based detectors is slow: a response time of nearly tens of microseconds makes most Gaussian shaping amplifiers (0.01–10 μs) unsuitable. The long response time is mainly caused by the unbalanced transport properties of electrons and holes in LHPSCs. Metal–semiconductor–metal structures with two Au (5.1 eV) electrodes could be a solution to achieve a majority carrier (hole-only) device. However, most of the charges from defects inside LHPSCs are holes, which may bury the signal from gamma-ray photons, and thus,

Received: January 9, 2024
Revised: February 14, 2024
Accepted: February 19, 2024
Published: February 27, 2024

ACS Publications

© 2024 American Chemical Society

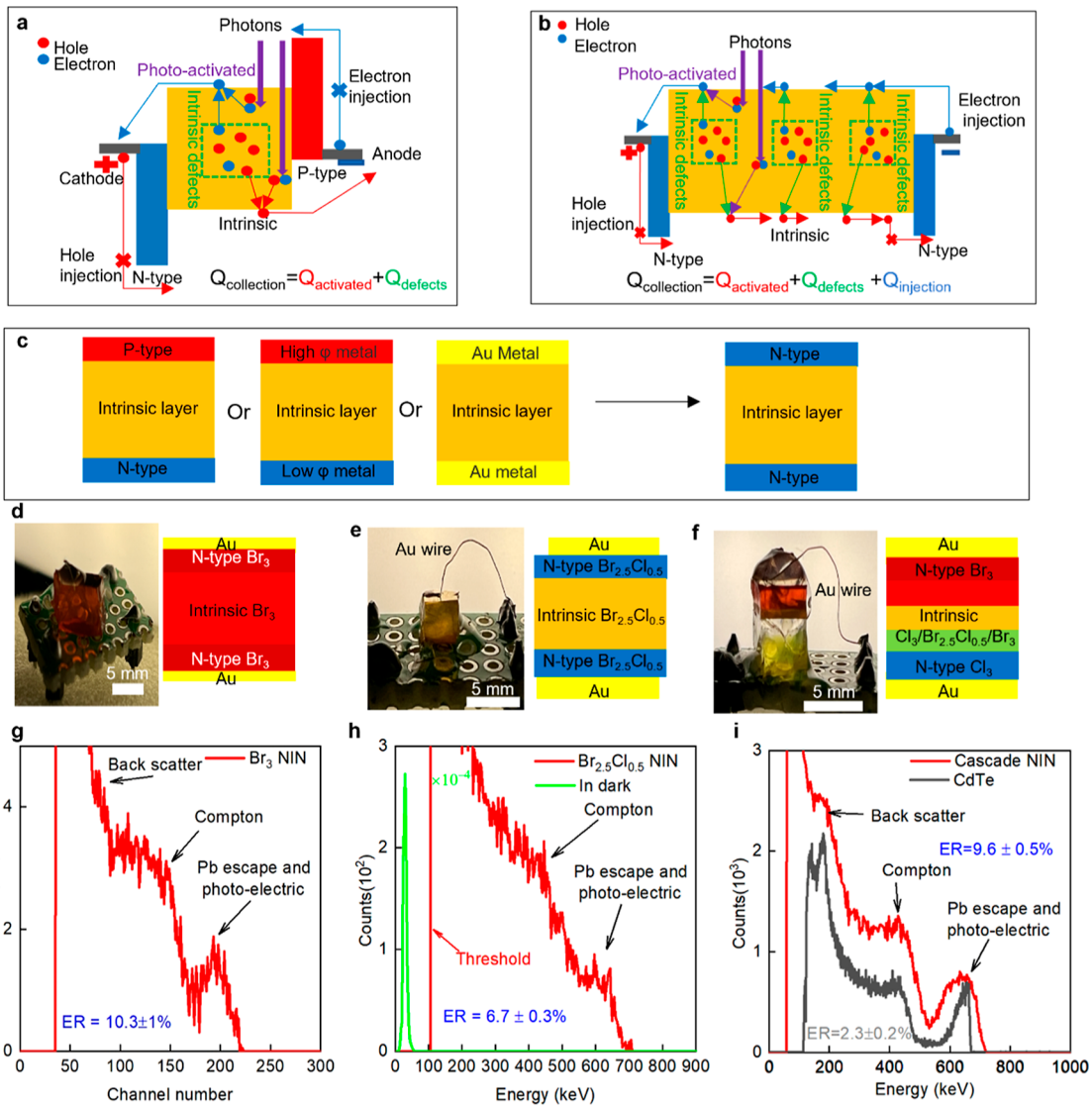

Figure 1. Gamma-ray detection of NIN photodiodes. (a) Mechanism of a PIN photodiode for photodetection. (b) Mechanism of an NIN photodiode for gamma-ray detection. (c) Electron–hole collection devices versus an electron-only collection device. (d) NIN photodiode made of $MAPbBr_3$ LHPSCs. (e) NIN photodiode made of $MAPbBr_{2.5}Cl_{0.5}$ LHPSCs. (f) NIN photodiode made of cascade LHPSCs with a halide gradient. (g) ^{137}Cs gamma-ray spectra resolved by a NIN photodiode made of $MAPbBr_3$ LHPSCs. (h) ^{137}Cs gamma-ray spectra resolved by an NIN photodiode made of $MAPbBr_{2.5}Cl_{0.5}$ LHPSCs. (i) ^{137}Cs gamma-ray spectra resolved by an NIN photodiode made of cascade LHPSCs and a CdTe single crystal.

it is urgent in the structure of an electron-only device to isolate the holes. When forming an electron-only MSM device, most low work function metals including Ag (4.28 eV) and Al (4.26 eV) would react with LHPSCs. As a result, using a heavily doped N-type layer to block the holes and form an electron-only device is an alternative method.

Herein, we consider the problem of intrinsic defects in solution processed LHPSCs and propose the isolation of noise from intrinsic defects inside LHPSCs by creating an energy barrier. Two n-type layers are symmetrically deposited on the opposite sides of intrinsic $MAPbX_3$ LHPSCs via solution-processed epitaxial growth.[22,23] Subsequently, unipolar photodiodes with an NIN structure are fabricated. Because the two n-type layers only allow the transport of electrons, the injection electrons, defect-induced electrons, and photon-activated electrons can contribute to the current. Conversely, the injection holes, defect-induced holes, and photon-activated holes would be suppressed. Therefore, by sacrificing the dark current, the holes from intrinsic defects can be suppressed and the response speed can be improved by abandoning the process of hole collection. Our devices comprising solution-processed $MAPbX_3$ LHPSCs with an NIN architecture have the ability to realize gamma-ray spectroscopy.

EXPERIMENTAL PROCEDURE

Materials. Lead bromide ($PbBr_2$; 99%), lead chloride ($PbCl_2$; 99%), methylammonium bromide (MABr), methylammonium chloride (MACl), bismuth bromide ($BiBr_3$; 99.9%), and bismuth chloride ($BiCl_3$; 99.9%) were purchased from Sigma-Aldrich, USA. Dimethyl sulfoxide (DMSO) and dimethylformamide-d7 (DMF-d7) were obtained from Aladdin. Metallic gold, silver, and gadolinium were purchased from Chinese reagent, China. All commercial products were used as received.

Growth of the NIN Photodiodes. For NIN photodiodes based on $MAPbBr_3$ and $MAPbBr_{2.5}Cl_{0.5}$ LHPSCs, high-quality $MAPbBr_3$ and $MAPbBr_{2.5}Cl_{0.5}$ LHPSCs were grown via inverse temperature crystallization, as previously reported.[23,24] Two n-type functional

https://doi.org/10.1021/acsami.4c00432
ACS Appl. Mater. Interfaces 2024, 16, 12106−12114

layers were epitaxially grown on the opposite faces of $MAPbBr_3$ and $MAPbBr_{2.5}Cl_{0.5}$ LHPSCs as two n-type layers. Subsequently, two Au electrodes were deposited on the opposite faces of Bi-doped $MAPbBr_3$ and Bidoped $MAPbBr_{2.5}Cl_{0.5}$ LHPSCs under a vacuum of 10^{-3} Pa. For the NIN photodiodes based on cascade LHPSCs, Bi-doped $MAPbCl_3$ LHPSCs were grown as substrates via inverse temperature crystallization. $MAPbCl_3$, $MAPbBr_{2.5}Cl_{0.5}$, $MAPbBr_3$, and Bi-doped $MAPbBr_3$ were formed stepwise through epitaxial growth. After the growth of Bi-doped $MAPbBr_3$, a diamond wire was used to cut the cascade LHPSCs to remove the useless surround parts. Then, the diamond powder dispersed in isopropanol was used as the polishing fluid to polish the faces of the cascade LHPSCs. Finally, two Au electrodes were deposited on the faces of Bi-doped $MAPbCl_3$ and Bi-doped $MAPbBr_3$ under a vacuum of 10^{-3} Pa.

Characterization of the LHPSCs and Photodiodes. X-ray diffraction (XRD) patterns were obtained using an X'TRA system with a Cu target (Switzerland). Scanning electron microscopy (SEM) images were obtained using a Quanta 200 FEI microscope. The samples for high-resolution transmission electron microscopy (HR-TEM) characterization were prepared via a focused ion beam (Helios 5 CX). The HR-TEM characterization was performed using a JEM-200CX transmission electron microscope (JEOL, Japan) with a high-voltage 220 kV beam. The Kelvin probe force microscopy probe station (Multimode-8-AM, USA) was used to measure the contact potential difference. Dark current density−voltage (J−V) characteristics were measured using a Keithley 4200 semiconductor analyzer (USA). The capacitance−voltage (C−V) characteristics were measured by a Keithley 4200 semiconductor analyzer with a very low frequency module. A 3000 Bq ^{137}Cs was used as the gamma-ray source.

Experiments with Gamma-Ray Photodiodes. The charge preamplifier was based on a CR-110 (rev 2.1) preamplifier from CREMAT (USA); the peripheral circuit was designed in-house. The shaping amplifiers, including CR-200 (1 and 8 μs) and the baseline restorer CR-210, were bought from CREMAT (USA). The high-voltage source (0−1500 V) was bought from Dongwen High Voltage (China). The multiple-channel analyzer (APG7300A) was bought from AP Holdings Co. (Japan).

RESULTS AND DISCUSSION

Figure 1a illustrates the charge collection process of a normal PIN photodiode. When a reverse bias is applied to the PIN photodiode, electrons and holes from the direct-current voltage source are blocked by the n- and p-type layers, respectively, resulting in a low dark current. Electron−hole pairs activated by photons in the intrinsic layer are separated by an electrical field; then, these charges drift to electrodes for collection as $Q_{activated}$ under bias. Nonetheless, the defects in the intrinsic layer randomly release charges that drift under an electrical field and are collected as $Q_{defects}$. On one hand, for the PIN photodiodes targeting visible photons, the thickness of the intrinsic layer is only ~1 μm to absorb all the visible photons. The defect density of the intrinsic layer is $\sim 10^9 \sim 10^{11}$ cm^{-3} for LHPSCs, resulting in a very low $Q_{defects}$.[25,26] On the other hand, the density of the incident photons is very large. Normally, $10^{12}-10^{20}$ visible photons would be absorbed in the intrinsic layer per second. Therefore, $Q_{activated}$ is in the range of $10^{-7}-10^{1}$ Coulomb. Consequently, the charges collected by PIN photodiodes due to absorbed visible photons are dominated by $Q_{activated}$.[27,28]

However, the gamma-ray to charges conversion process is completely different. Owing to the strong penetrating ability of gamma-ray photons, a thickness of millimeters or even centimeters is required for sufficient energy deposition. Thus, for a 1 cm thick active layer based on an LHPSC, the $Q_{defects}$ value is 10^4 times larger than that for PIN photodiodes for visible photons. Moreover, the charges activated by a single 662 keV photon are only ~0.05 pC (10^7-10^{14} times smaller than the charges associated with visible photons). $Q_{activated}$ in thick gamma-ray photodiodes is much smaller than $Q_{activated}$ for the PIN photodiodes for visible photons. Therefore, most solution-processed LHPSCs may show great performance in the detection of visible photons, but for gamma-ray detection, most solution-processed LHPSCs can only identify the number of photon peaks and cannot achieve gamma-ray spectroscopy with good energy resolution.[29−31] Except of improving the crystallization of LHPSCs with fewer defects, designing a band-energy barrier is imperative to further suppress the contribution of intrinsic defects for low-noise gamma-ray photodiodes.[32,33]

As shown in Figure 1b, the P-type layer in a PIN photodiode is replaced by an N-type layer to form an NIN photodiode. In the structure of the NIN photodiode, the defect-induced, photon-activated, and injected holes are suppressed by the symmetrical blocking layers. Thus, the large $Q_{defects}$ value could be reduced for the LHPSCs, which mainly contain hole defects. Although the signal of holes is sacrificed, the very large thickness of the intrinsic layer could still suppress the dark current with high resistance to some extent, resulting in a relatively low $Q_{injection}$. In particular, a large and stable dark current would not cause sufficient charge integration and cannot contribute to photon peaks. Further, abandoning the photon-activated holes could improve the response speed. A shorter response time could not only improve the maximum count rate of detectors for gamma-ray photons but also suppress the noise charges during the event.

Figure 1c shows three types of photodiodes: a PIN-type photodiode made of n-type/intrinsic/p-type layers, a Schottky photodiode made of asymmetric electrodes, and back-to-back symmetrical electrodes.[14,34−39] No devices made of LHPSCs can reduce the noise from intrinsic defects in LHPSCs. For our NIN photodiodes, we aim to use symmetric N-type layers to block the noise due to defect-induced holes.

Figure 1d shows the $MAPbBr_3$ LHPSC-based NIN photodiodes with an architecture of Au/(Bi-doped $MAPbBr_3$)/(intrinsic $MAPbBr_3$)/(Bi-doped $MAPbBr_3$)/Au.[40−43] The thickness of the two N-type layers is ~100 μm, and the thickness of the intrinsic $MAPbBr_3$ is 6.8 mm (6.5 mm in length and 2.4 mm in width). Similarly, an $MAPbBr_{2.5}Cl_{0.5}$ LHPSC-based NIN photodiode with a structure of Au/(Bi-doped $MAPbBr_{2.5}Cl_{0.5}$)/(intrinsic $MAPbBr_{2.5}Cl_{0.5}$)/(Bi-doped $MAPbBr_{2.5}Cl_{0.5}$)/Au is shown in Figure 1e; the thickness of the intrinsic $MAPbBr_{2.5}Cl_{0.5}$ is 3.8 mm (3.5 mm in length and 2.4 mm in width). In particular, the cascade LHPSC of $MAPbCl_3$/$MAPbBr_{2.5}Cl_{0.5}$/$MAPbBr_3$ with a halide gradient also acts as an intrinsic layer (Figure 1f). Bi-doped $MAPbCl_3$ and Bi-doped $MAPbBr_3$ LHPSCs (4.1 mm in length and 3.9 mm in width) are used as n-type layers and form homojunctions. The thicknesses of each layer are 3.8, 0.9, 0.8, 2.0, and 0.1 mm for Bi-doped $MAPbCl_3$, $MAPbCl_3$, $MAPbBr_{2.5}Cl_{0.5}$, $MAPbBr_3$, and Bidoped $MAPbBr_3$, respectively. More information about the N-type layer and intrinsic layer is obtained from the Hall effect, as shown in Figure S1 and Table S1.

Figure 1g shows the ^{137}Cs gamma-ray spectrum resolved by $MAPbBr_3$ LHPSC-based NIN photodiodes with a shaping time of 8 μs. Under an external bias of 300 V, our $MAPbBr_3$ LHPSC-based NIN photodiodes achieve an energy resolution of 10.3% for ^{137}Cs 662 keV gamma-ray photons. Owing to the occurrence of the Pb escape peak being very close to the

https://doi.org/10.1021/acsami.4c00432
ACS Appl. Mater. Interfaces 2024, 16, 12106−12114

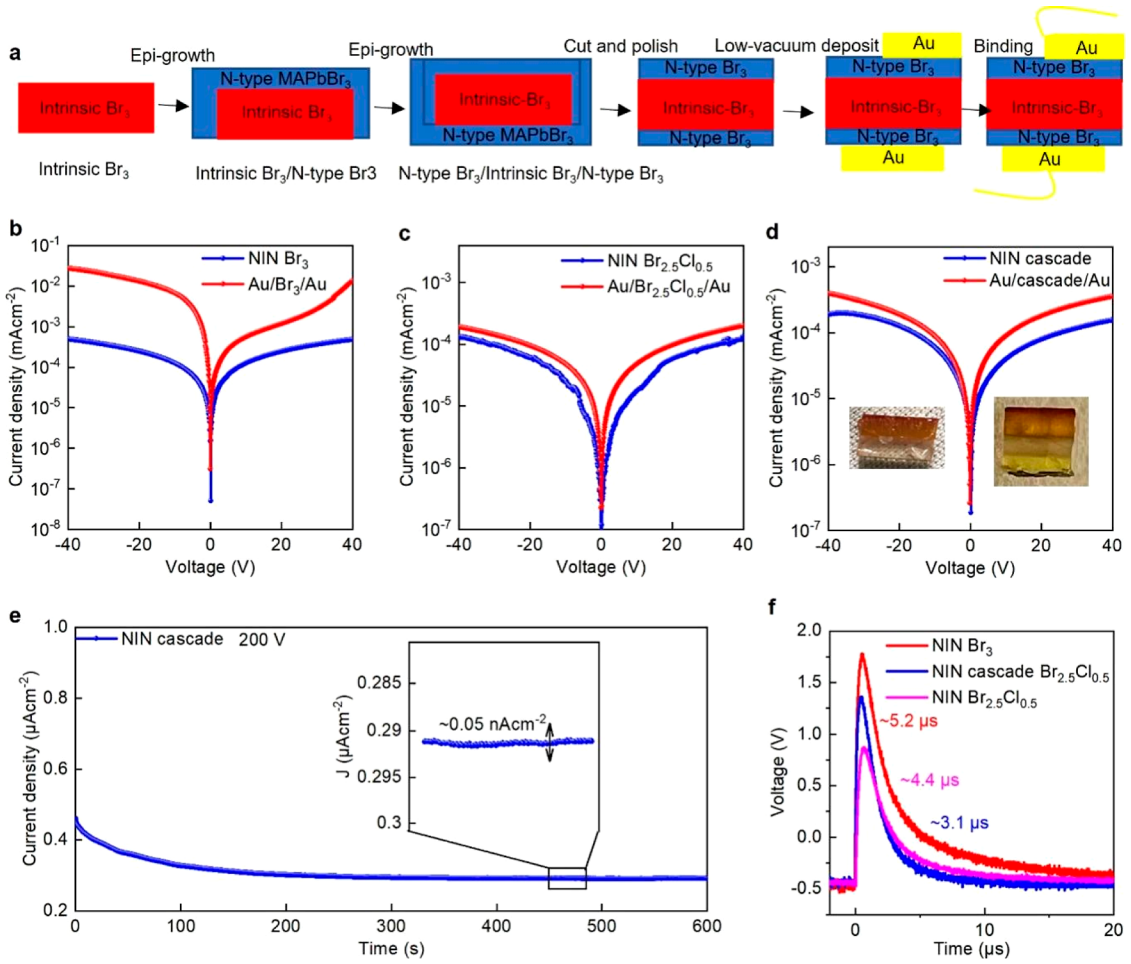

Figure 2. Characteristics of the NIN photodiodes. (a) Fabrication process of the NIN photodiodes. (b) Current density−voltage curves of NIN photodiodes based on the $MAPbBr_3$ LHPSC and Au/$MAPbBr_3$ LHPSC/Au. (c) Current density−voltage curve of NIN photodiodes based on the $MAPbBr_{2.5}Cl_{0.5}$ LHPSC and Au/$MAPbBr_{2.5}Cl_{0.5}$ LHPSC/Au. (d) Current density−voltage curve of NIN photodiodes based on the cascade LHPSC and Au/cascade LHPSC/Au. (e) Current density−time curve of the NIN photodiode based on the cascade LHPSC. (f) Response time of the three types of NIN photodiodes.

photoelectrical peak, which causes serious broadening of the photoelectrical peak, we are unable to discriminate these peaks at this stage.[13] However, the gamma-ray spectrum from an NIN photodiode is much better resolved compared with that of a PIN photodiode (Figure S2). When we replaced the $MAPbBr_3$ LHPSC with the $MAPbBr_{2.5}Cl_{0.5}$ LHPSC, we still achieved an acceptable energy resolution of 6.7% for ^{137}Cs 662 keV gamma-ray photons and the noise signal in the dark in below the threshold (Figure 1h). Two peaks that are located near the high-energy channel could be the Pb escape peak and the photoelectrical peak when we enlarge the small peaks of the large channel (Figure S3). Furthermore, we replaced the individual $MAPbBr_3$ layer with an LHPSC containing a halide gradient for fabricating NIN photodiodes. Because the built-in potential of a halide gradient could improve the charge collection efficiency, an energy resolution of 9.6% was achieved for ^{137}Cs 662 keV gamma-ray photons.[23,44] In addition, we compared our NIN photodiode with a high-quality CdTe single crystal (an energy resolution of ∼2.4%, provided by Acrorad). To the best of our knowledge, this is the first report of an $MAPbBr_3$ LHPSC achieving an acceptable resolution of ^{137}Cs gamma-ray photons. Moreover, the results demonstrate that the structure of NIN photodiodes could motivate the development of three types of LHPSCs to resolve gamma-ray photons. And the reproducibility of our NIN photodiodes is further investigated in Figure S4.

To understand the advantages of NIN photodiodes, we compared their electrical properties with those of an Au/LHPSC/Au structure. Figure 2a shows the facile fabrication process of our NIN photodiodes. For example, a high-quality intrinsic $MAPbBr_3$ LHPSC was first used as the substrate. Then, a Bi-doped $MAPbBr_3$ LHPSC was grown on the top face of the intrinsic $MAPbBr_3$ LHPSC substrate. Subsequently, we flipped the device over, and the Bi-doped $MAPbBr_3$ LHPSC was further grown on the bottom face of the intrinsic $MAPbBr_3$ LHPSC substrate. Because the Bi-doped $MAPbBr_3$ LHPSC would also grow on the side faces of the intrinsic $MAPbBr_3$ LHPSC, a diamond wire was used to remove the useless parts and polish the shear to suppress the surface charges. Then, two Au electrodes with a thickness of 100 nm were deposited on the opposite faces of the LHPSC. Finally, two Au wires were used to connect the electrodes to the peripheral circuit.

To evaluate the dark current of our NIN photodiodes, the current density versus voltage curve was measured for $MAPbBr_3$ LHPSC-based NIN photodiodes (Figure 2b). Our NIN photodiode exhibits a lower dark current density (0.7 μA cm^{-2}) than that of Au/$MAPbBr_3$ LHPSC/Au (12 μA cm^{-2}) at −40 V. The NIN photodiodes could suppress the current

https://doi.org/10.1021/acsami.4c00432
ACS Appl. Mater. Interfaces 2024, 16, 12106−12114

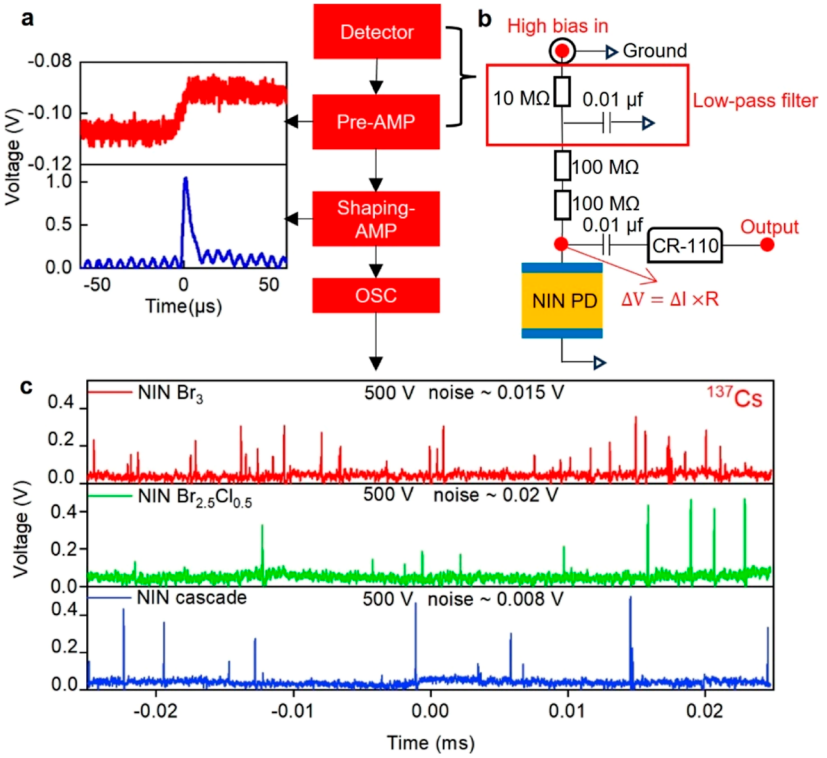

Figure 3. (a) ^{137}Cs gamma-ray single photon counting by an NIN photodiode. (b) Access circuit of the NIN photodiodes in the preamplifier. (c) ^{137}Cs gamma-ray response after applying the shaping amplifier (8 μs) to the three types of NIN photodiodes.

contribution of the injection holes and the holes from intrinsic defects, considerably reducing the number of charges transported through the NIN photodiodes. Nevertheless, the dark current density of NIN photodiodes is much higher than that of the PIN photodiodes, in the order of tens of nanoamperes.[16,17] For the $MAPbBr_{2.5}Cl_{0.5}$ LHPSC-based NIN photodiodes (Figure 2c), the dark current density is measured to be 120 nA cm^{-2} at −40 V, which is slightly lower than that of Au/$MAPbBr_{2.5}Cl_{0.5}$ LHPSC/Au (190 nA cm^{-2} at −40 V). Because the $MAPbBr_{2.5}Cl_{0.5}$ LHPSC owns fewer defects than the $MAPbBr_3$ LHPSC, fewer defect-induced holes exist in the $MAPbBr_{2.5}Cl_{0.5}$ LHPSC. Figure 2d shows the J−V characterization of the cascade LHPSC-based NIN photodiode, for which the dark current density is 210 nA cm^{-2} at −40 V, whereas the dark current density of Au/cascade LHPSC/Au is 410 nA cm^{-2} at −40 V. Therefore, the NIN photodiodes could reduce the dark current by suppressing the number of injection holes and defect-induced holes.

In addition to the study of the dark current under bias, the study of the stability or fluctuations of the dark current is of primary importance. As shown in Figure 2e, a bias of 200 V is applied to the cascade NIN photodiode for 600 s. The initial dark current density of the photodiode is 440 nA cm^{-2} and it decreases continuously to 292 nA cm^{-2} after 300 s, at which point it becomes stable. The fluctuation of the dark current density caused by the polarization of charges and halide ions inside the device is < 0.05 nA cm^{-2}. Here, the dark current density of our NIN photodiodes is very large compared to that of CdZnTe single crystals. However, the stable dark current would result in a very low noise because only the coupling capacitance only allow the pulse signal to pass through. A more exaggerated experiment about the dark current is shown in Figure S5. And the junction capacitances of our NIN photodiodes are measured to be 4.5 pF, 5.2 pF, and 23 pF for $MAPbBr_3$ LHPSC, $MAPbBr_{2.5}Cl_{0.5}$ LHPSC, and cascade LHPSC (200 V)-based NIN photodiodes, respectively, at 10 Hz (Figure S6).

Because only electrons can be transported throughout the NIN photodiodes, the response speed of the NIN photodiodes with different intrinsic layers is investigated in Figure 2f. Using a 350 nm pulsed laser with a width of 7 ns as the light source, the response speeds of the $MAPbBr_3$ LHPSC (200 V), $MAPbBr_{2.5}Cl_{0.5}$ LHPSC (200 V), and cascade LHPSC (200 V)-based NIN photodiodes are measured to be 5.2, 4.4, and 3.1 μs, respectively. Besides, the response speed for α particle is fast enough for the Gaussian shaping amplifier to integrate all the charges, as shown in Figure S7.

The performance of the cascade LHPSC-based NIN photodiodes for individual ^{137}Cs 662 keV gamma-ray photons was then investigated. An example of the obtained single gamma-ray photon signal traces using a preamplifier (red) and a Gaussian shaping amplifier (blue) is shown in Figure 3a.

Then, the access circuit of the NIN photodiodes and the preamplifier is shown in Figure 3b. The high bias would first come across a low-pass filter for stable direct-current bias and then encounter two resistances (100 MΩ) to acquire a tiny variation of the photoinduced current. Because only the alternating current signal could transport through the capacitance, the direct-current dark current would not contribute to the output. Figure 3c shows the trace of the NIN photodiodes comprising different intrinsic layers. When a ^{137}Cs 662 keV gamma-ray photon is incident onto the NIN photodiodes, a photo peak would be recorded by the oscilloscope with a time duration of 50 ms. At this stage, we can directly determine the detection performance of the gamma-ray detector. The preamplifier converts 1 pC into 1.4

https://doi.org/10.1021/acsami.4c00432
ACS Appl. Mater. Interfaces 2024, 16, 12106−12114

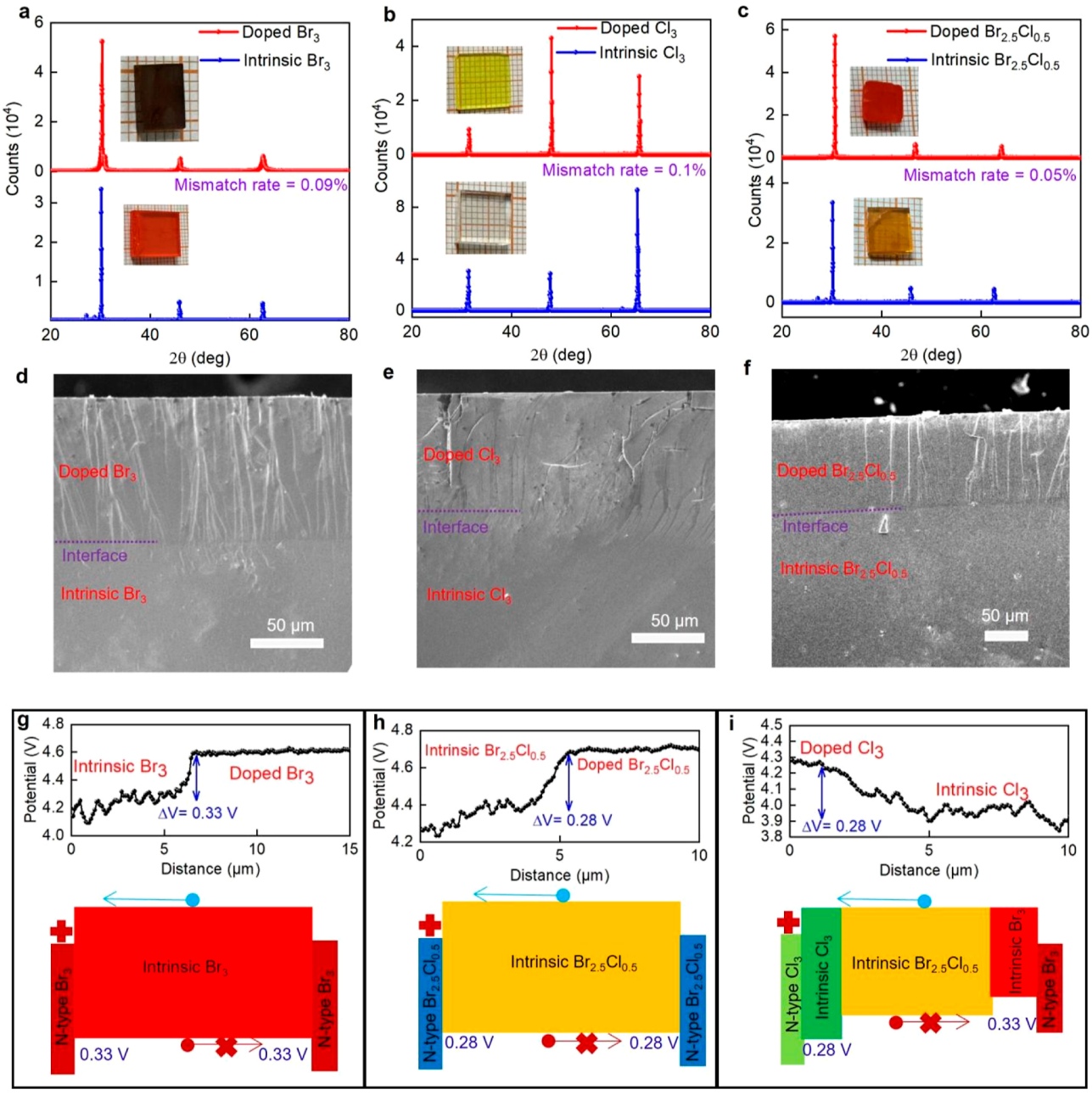

Figure 4. Characterization of the homojunctions of NIN photodiodes. (a) X-ray diffraction spectra of the doped $MAPbBr_3$ LHPSC and intrinsic $MAPbBr_3$ LHPSC. (b) X-ray diffraction spectra of the doped $MAPbCl_3$ LHPSC and intrinsic $MAPbCl_3$ LHPSC. (c) X-ray diffraction spectra of the doped $MAPbBr_{2.5}Cl_{0.5}$ LHPSC and intrinsic $MAPbBr_{2.5}Cl_{0.5}$ LHPSC. (d) Interface cross-section of (doped $MAPbBr_3$ LHPSC)/(intrinsic $MAPbBr_3$ LHPSC). (e) Interface cross-section of (doped $MAPbCl_3$ LHPSC)/(intrinsic $MAPbCl_3$ LHPSC). (f) Interface cross-section of (doped $MAPbBr_{2.5}Cl_{0.5}$ LHPSC)/(intrinsic $MAPbBr_{2.5}Cl_{0.5}$ LHPSC). (g) Interface potential profile of (doped $MAPbBr_3$ LHPSC)/(intrinsic $MAPbBr_3$ LHPSC). (h) Interface potential profile of (doped $MAPbBr_{2.5}Cl_{0.5}$ LHPSC)/(intrinsic $MAPbBr_{2.5}Cl_{0.5}$ LHPSC). (i) Interface potential profile of (doped $MAPbCl_3$ LHPSC)/(intrinsic $MAPbCl_3$ LHPSC).

V, and the shaping amplifier amplifies the signal by a factor of 10. The voltage fluctuation of 0.015 V for the NIN photodiode based on an $MAPbBr_3$ LHPSC represents a noise level of ~650 electrons at 500 V bias. In comparison, the noise level is as low as ~860 and ~340 electrons for $MAPbBr_{2.5}Cl_{0.5}$ and cascade LHPSC-based NIN photodiodes, respectively. When a 662 keV gamma-ray photon is incident onto the NIN photodiodes, the largest responses are approximately 1.3×10^4, 1.7×10^4, and 2.4×10^4 electrons. When the electron−hole pair ionization energy is ~6 eV, 5.5×10^4 electrons are activated during one event. Thus, the electron collection efficiency for NIN photodiodes based on LHPSCs is 23−43%. And the comparison of our NIN photodiodes with the previous reported work is shown in Table S2.

The interfaces of the homojunctions are investigated to understand the extremely low noise of hundreds of electrons. To form sufficient and low-defect interfaces, the lattice mismatch rate should be as low as possible. Figure 4a shows the XRD spectra of the doped $MAPbBr_3$ and intrinsic $MAPbBr_3$ LHPSCs. According to the Bragg equation, the lattice constants of the doped $MAPbBr_3$ and intrinsic $MAPbBr_3$ LHPSCs are 5.906 and 5.917 Å, respectively,

https://doi.org/10.1021/acsami.4c00432
ACS Appl. Mater. Interfaces 2024, 16, 12106−12114

resulting in a mismatch rate of 0.09%, which could significantly avoid the inclusion of defects near interfaces.[45] Furthermore, the mismatch rates for the interfaces of (doped $MAPbCl_3$)/(intrinsic $MAPbCl_3$) and (doped $MAPbBr_{2.5}Cl_{0.5}$)/(intrinsic $MAPbBr_{2.5}Cl_{0.5}$) are only 0.1 and 0.05%, respectively, as shown in Figure 4b,c. The interface near the intrinsic layer and N-type function layer is further investigated via SEM (Figure 4d−f). An N-type layer with a thickness of ∼100 μm is epitaxially grown on the intrinsic substrate with a continuous and flat interface. A high-resolution TEM image of the interface is shown in Figure S8. To further confirm the band structure of our NIN photodiodes, the cross-sections of the homojunctions are investigated using a Kelvin force probe for obtaining the potential profile. As shown in Figure 4g, an abrupt potential change of 0.33 V is observed near the interface of (doped $MAPbBr_3$)/(intrinsic $MAPbBr_3$), which could prevent the drifting of holes in the intrinsic layer into the electrodes. For the interfaces of (doped $MAPbBr_{2.5}Cl_{0.5}$)/(intrinsic $MAPbBr_{2.5}Cl_{0.5}$) and (doped $MAPbCl_3$)/(intrinsic $MAPbCl_3$), the potentials vary by 0.28 and 0.33 V, respectively, as shown in Figure 4hi. Based on the Kelvin force microscopy results, we can sketch the energy diagram, finding that the energy barriers can sufficiently block the holes.

CONCLUSIONS

The main hindrance to the gamma-ray detection performance of $MAPbX_3$ LHPSCs with a large thickness is the noise generated by the intrinsic defects. Therefore, herein, we report a facile method to fabricate photodiodes with an NIN structure via solution-processed epitaxial growth. The lattice-matched homojunctions can sufficiently avoid the interface-induced defects. Therefore, we used the $MAPbBr_3$ LHPSC for the first time to resolve 662 keV ^{137}Cs gamma-ray photons. The results obtained for the NIN structure of this LHPSC could also motivate the development of gamma-ray detectors based on other types of $MAPbX_3$ LHPSCs. This study presents a major advancement in room-temperature semiconductor gamma-ray detectors based on solution-processed single crystals.

ASSOCIATED CONTENT

Supporting Information

The Supporting Information is available free of charge at https://pubs.acs.org/doi/10.1021/acsami.4c00432.

Setup of the Hall effect experiments, the results of the Hall effect experiments including the mobility, charges type and density of different LHPSCs, the gamma-ray response of a PIN photodiode made of $MAPbBr_3$, the gamma-ray response of an NIN photodiode made of $MAPbBr_{2.5}Cl_{0.5}$ with different scales, gamma-ray response of NIN photodiodes with different samples, the Schottky diode made of the CdTe single crystal for gamma-ray detection, C−V results of different NIN photodiodes, response speed measured by alpha particles, the HR-TEM image of the interface near (intrinsic $MAPbBr_3$)/(n-type $MAPbBr_3$ LHPSC), and the comparison with the previous reported work PDF

AUTHOR INFORMATION

Corresponding Authors

Xin Wang − *School of Electronic Science and Engineering, Southeast University, Nanjing 210000, China;* orcid.org/0000-0003-2496-2872; Email: xinw@seu.edu.cn

Wei Lei − *School of Electronic Science and Engineering, Southeast University, Nanjing 210000, China*; Email: lw@seu.edu.cn

Xiaobao Xu − *School of Electronic Science and Engineering, Southeast University, Nanjing 210000, China;* orcid.org/0000-0001-5378-5604; Email: xiaobaoxu@seu.edu.cn

Authors

Yubing Xu − *School of Electronic Science and Engineering, Southeast University, Nanjing 210000, China*

Yuzhu Pan − *School of Electronic Science and Engineering, Southeast University, Nanjing 210000, China*

Shunjie Chai − *School of Electronic Science and Engineering, Southeast University, Nanjing 210000, China*

Jie Wu − *School of Electronic Science and Engineering, Southeast University, Nanjing 210000, China*

Jingda Zhao − *School of Electronic Science and Engineering, Southeast University, Nanjing 210000, China*

Yuwei Li − *School of Electronic Science and Engineering, Southeast University, Nanjing 210000, China*

Zhiwei Zhao − *School of Electronic Science and Engineering, Southeast University, Nanjing 210000, China*

Qing Li − *School of Electronic Science and Engineering, Southeast University, Nanjing 210000, China*

Jun Wu − *School of Electronic Science and Engineering, Southeast University, Nanjing 210000, China;* orcid.org/0000-0002-9912-5238

Jing Chen − *School of Electronic Science and Engineering, Southeast University, Nanjing 210000, China;* orcid.org/0000-0001-6703-2486

Byung Seong Bae − *Department of Electronics &Display Engineering, Hoseo University, Asan City, Chungnam 31499, Republic of Korea;* orcid.org/0000-0002-3328-0286

Jianming Zhou − *E-xray Electronic Co. Ltd., Suzhou 215131, China*

Ying Zhu − *E-spectrum Optoelectronic Co. Ltd., Suzhou 215111, China*

Complete contact information is available at: https://pubs.acs.org/10.1021/acsami.4c00432

Author Contributions

The manuscript was written through contributions of all authors. All authors have given approval to the final version of the manuscript.

Notes

The authors declare no competing financial interest.

ACKNOWLEDGMENTS

This work was financially supported by the National Natural Science Foundation (12005038 and 12375306), China Postdoctoral Foundation funded project (2023T160106 and 2023M730555), National Key Research and Development Program of China (2021YFE0105900 and 2022YFE0139100), National Natural Science Foundation Project of China (62175028, 51879042, and 61674029), Program 111_2.0 in China (BP0719013), Leading Technology of Jiangsu Basic Research Plan (BK20192003), and International cooperative research project of Jiangsu province (BZ2022008).

REFERENCES

(1) Andricevic, P.; Frajtag, P.; Lamirand, V. P.; Pautz, A.; Kollar, M.; Nafradi, B.; Sienkiewicz, A.; Garma, T.; Forro, L.; Horvath, E.

Kilogram-Scale Crystallogenesis of Halide Perovskites for Gamma-Rays Dose Rate Measurements. *Adv. Sci.* **2021**, *8*, 2001882.
(2) Zhang, Z.; Yang, G. Recent Advancements in Using Perovskite Single Crystals for Gamma-Ray Detection. *J. Mater. Sci.: Mater. Electron.* **2021**, *32*, 12758−12770.
(3) Baussens, O.; Montémont, G.; Verilhac, J. M.; Hirsch, L.; Gros-Daillon, E. Noise Spectroscopy Study of Methylammonium Lead Tribromide Single-Crystal Detectors: Gamma-Ray Spectroscopy Applications. *Nucl. Instrum. Methods Phys. Res., Sect. A* **2022**, *1038*, 166904.
(4) Pan, L.; Feng, Y.; Kandlakunta, P.; Huang, J.; Cao, L. R. Performance of Perovskite $CsPbBr_3$ Single Crystal Detector for Gamma-Ray Detection. *IEEE Trans. Nucl. Sci.* **2020**, *67*, 443−449.
(5) Roy, U. N.; Bolotnikov, A. E.; Camarda, G. S.; Cui, Y.; Hossain, A.; Lee, K.; Marshall, M.; Yang, G.; James, R. B. Growth of $CdTe_xSe_{1-x}$ from a Te-Rich Solution for Applications in Radiation Detection. *J. Cryst. Growth* **2014**, *386*, 43−46.
(6) Sato, G.; Fukuyama, T.; Watanabe, S.; Ikeda, H.; Ohta, M.; Ishikawa, S. n.; Takahashi, T.; Shiraki, H.; Ohno, R. Study of Polarization Phenomena in Schottky CdTe Diodes Using Infrared Light Illumination. *Nucl. Instrum. Methods Phys. Res., Sect. A* **2011**, *652*, 149−152.
(7) Iwanczyk, J. S.; Nygard, E.; Meirav, O.; Arenson, J.; Barber, W. C.; Hartsough, N. E.; Malakhov, N.; Wessel, J. C. Photon Counting Energy Dispersive Detector Arrays for X-Ray Imaging. *IEEE Trans. Nucl. Sci.* **2009**, *56*, 535−542.
(8) Xu, L.; Zhou, Y.; Fu, X.; Liang, L.; Jie, W. Hydrogen Passivation of Defect Levels in the Annealed CdZnTe:In Crystals. *J. Mater. Res.* **2020**, *35*, 3041−3047.
(9) Szeles, C.; Soldner, S. A.; Vydrin, S.; Graves, J.; Bale, D. S. CdZnTe Semiconductor Detectors for Spectroscopic X-Ray Imaging. *IEEE Trans. Nucl. Sci.* **2008**, *55*, 572−582.
(10) Veale, M. C.; Booker, P.; Cross, S.; Hart, M. D.; Jowitt, L.; Lipp, J.; Schneider, A.; Seller, P.; Wheater, R. M.; Wilson, M. D.; Hansson, C. C. T.; Iniewski, K.; Marthandam, P.; Prekas, G. Characterization of the Uniformity of High-Flux CdZnTe Material. *Sensors* **2020**, *20*, 2747.
(11) Zhao, L.; Zhou, Y.; Shi, Z.; Ni, Z.; Wang, M.; Liu, Y.; Huang, J. High-Yield Growth of $FACsPbBr_3$ Single Crystals with Low Defect Density from Mixed Solvents for Gamma-Ray Spectroscopy. *Nat. Photonics* **2023**, *17*, 315−323.
(12) Liu, X.; Xu, M.; Hao, Y.; Fu, J.; Wang, F.; Zhang, B.; Bennett, S.; Sellin, P.; Jie, W.; Xu, Y. Solution-Grown Formamidinium Hybrid Perovskite $FAPbBr_3$ Single Crystals for Alpha-Particle and Gamma-Ray Detection at Room Temperature. *ACS Appl. Mater. Interfaces* **2021**, *13*, 15383−15390.
(13) Liu, F.; Yoho, M.; Tsai, H.; Fernando, K.; Tisdale, J.; Shrestha, S.; Baldwin, J. K.; Mohite, A. D.; Tretiak, S.; Vo, D. T.; Nie, W. The Working Principle of Hybrid Perovskite Gamma-Ray Photon Counter. *Mater. Today* **2020**, *37*, 27−34.
(14) Wei, H.; DeSantis, D.; Wei, W.; Deng, Y.; Guo, D.; Savenije, T. J.; Cao, L.; Huang, J. Dopant Compensation in Alloyed $CH_3NH_3PbBr_{3-x}Cl_x$ Perovskite Single Crystals for Gamma-Ray Spectroscopy. *Nat. Mater.* **2017**, *16*, 826−833.
(15) Liu, Y.; Zhang, Y.; Zhu, X.; Feng, J.; Spanopoulos, I.; Ke, W.; He, Y.; Ren, X.; Yang, Z.; Xiao, F.; Zhao, K.; Kanatzidis, M. G.; Liu, S. F. Triple-Cation and Mixed-Halide Perovskite Single Crystal for High-Performance X-Ray Imaging. *Adv. Mater.* **2021**, *33*, 2006010.
(16) Wang, X.; Xu, Y.; Pan, Y.; Li, Y.; Xu, J.; Chen, J.; Wu, J.; Li, Q.; Zhang, X.; Zhao, Z.; Li, C.; Elemike, E. E.; Onwudiwe, D. C.; Akram, J.; Lei, W. Low-Noise X-Ray PIN Photodiodes Made of Perovskite Single Crystals by Solution-processed Dopant Incorporated Epitaxial Growth. *Nano Energy* **2021**, *89*, 106311.
(17) Xu, Q.; Wang, X.; Zhang, H.; Shao, W.; Nie, J.; Guo, Y.; Wang, J.; Ouyang, X. $CsPbBr_3$ Single Crystal X-Ray Detector with Schottky Barrier for X-Ray Imaging Application. *ACS Appl. Electron. Mater.* **2020**, *2*, 879−884.
(18) Yao, F.; Peng, J.; Li, R.; Li, W.; Gui, P.; Li, B.; Liu, C.; Tao, C.; Lin, Q.; Fang, G. Room-Temperature Liquid Diffused Separation Induced Crystallization for High-Quality Perovskite Single Crystals. *Nat. Commun.* **2020**, *11*, 1194.
(19) Liu, Y.; Zhang, Y.; Zhu, X.; Yang, Z.; Ke, W.; Feng, J.; Ren, X.; Zhao, K.; Liu, M.; Kanatzidis, M. G.; Liu, S. Inch-Sized High-Quality Perovskite Single Crystals by Suppressing Phase Segregation for Light-Powered Integrated Circuits. *Sci. Adv.* **2021**, *7*, No. eabc8844.
(20) Geng, X.; Feng, Q.; Zhao, R.; Hirtz, T.; Dun, G.; Yan, Z.; Ren, J.; Zhang, H.; Liang, R.; Tian, H.; Xie, D.; Yang, Y.; Ren, T. High-Quality Single Crystal Perovskite for Highly Sensitive X-Ray Detector. *IEEE Electron Device Lett.* **2020**, *41*, 256−259.
(21) Wei, H.; Huang, J. Halide Lead Perovskites for Ionizing Radiation Detection. *Nat. Commun.* **2019**, *10*, 1066.
(22) Wang, X.; Pan, Y.; Xu, Y.; Zhao, J.; Li, Y.; Li, Q.; Chen, J.; Zhao, Z.; Zhang, X.; Elemike, E. E.; Onwudiwe, D. C.; Bae, B. S.; Lei, W. High Spectral-Rejection-Ratio Narrowband Photodetectors Based on Perovskite Heterojunctions. *Adv. Electron. Mater.* **2022**, *8*, 2200178.
(23) Wang, X.; Li, Y.; Xu, Y.; Pan, Y.; Zhu, C.; Zhu, D.; Wu, Y.; Li, G.; Zhang, Q.; Li, Q.; Zhang, X.; Wu, J.; Chen, J.; Lei, W. Solution-Processed Halide Perovskite Single Crystals with Intrinsic Compositional Gradients for X-Ray Detection. *Chem. Mater.* **2020**, *32*, 4973−4983.
(24) Saidaminov, M. I.; Abdelhady, A. L.; Murali, B.; Alarousu, E.; Burlakov, V. M.; Peng, W.; Dursun, I.; Wang, L.; He, Y.; Maculan, G.; Goriely, A.; Wu, T.; Mohammed, O. F.; Bakr, O. M. High-quality Bulk Hybrid Perovskite Single Crystals Within Minutes by Inverse Temperature Crystallization. *Nat. Commun.* **2015**, *6*, 7586.
(25) Liu, Y.; Zhang, Y.; Zhao, K.; Yang, Z.; Feng, J.; Zhang, X.; Wang, K.; Meng, L.; Ye, H.; Liu, M.; Liu, S. A 1300 mm^2 Ultrahigh-Performance Digital Imaging Assembly using High-Quality Perovskite Single Crystals. *Adv. Mater.* **2018**, *30*, 1707314.
(26) Cheng, Z.; Liu, K.; Yang, J.; Chen, X.; Xie, X.; Li, B.; Zhang, Z.; Liu, L.; Shan, C.; Shen, D. High-Performance Planar-Type Ultraviolet Photodetector Based on High-Quality $CH_3NH_3PbCl_3$ Perovskite Single Crystals. *ACS Appl. Mater. Interfaces* **2019**, *11*, 34144−34150.
(27) Lei, Y.; Chen, Y.; Zhang, R.; Li, Y.; Yan, Q.; Lee, S.; Yu, Y.; Tsai, H.; Choi, W.; Wang, K.; Luo, Y.; Gu, Y.; Zheng, X.; Wang, C.; Wang, C.; Hu, H.; Li, Y.; Qi, B.; Lin, M.; Zhang, Z.; Dayeh, S. A.; Pharr, M.; Fenning, D. P.; Lo, Y. H.; Luo, J.; Yang, K.; Yoo, J.; Nie, W.; Xu, S. A Fabrication Process for Flexible Single-Crystal Perovskite Devices. *Nature* **2020**, *583*, 790−795.
(28) Gao, Y.; Cansizoglu, H.; Polat, K. G.; Ghandiparsi, S.; Kaya, A.; Mamtaz, H. H.; Mayet, A. S.; Wang, Y.; Zhang, X.; Yamada, T.; Devine, E. P.; Elrefaie, A. F.; Wang, S.; Islam, M. S. Photon-Trapping Microstructures Enable High-Speed High-Efficiency Silicon Photodiodes. *Nat. Photonics* **2017**, *11*, 301−308.
(29) Li, L.; Chen, H.; Fang, Z.; Meng, X.; Zuo, C.; Lv, M.; Tian, Y.; Fang, Y.; Xiao, Z.; Shan, C.; Xiao, Z.; Jin, Z.; Shen, G.; Shen, L.; Ding, L. An Electrically Modulated Single-Color/Dual-Color Imaging Photodetector. *Adv. Mater.* **2020**, *32*, 1907257.
(30) Xie, C.; You, P.; Liu, Z.; Li, L.; Yan, F. Ultrasensitive Broadband Phototransistors based on Perovskite/Organic-semiconductor Vertical Heterojunctions. *Light: Sci. Appl.* **2017**, *6*, 17023.
(31) Yang, T.; Li, F.; Zheng, R. Recent Progress on Cesium Lead Halide Perovskites for Photodetection Applications. *ACS Appl. Electron. Mater.* **2019**, *1*, 1348−1366.
(32) Klepov, V. V.; De Siena, M. C.; Pandey, I. R.; Pan, L.; Bayikadi, K. S.; Butun, S.; Chung, D. Y.; Kanatzidis, M. G. Laser Scribing for Electrode Patterning of Perovskite Spectrometer-Grade $CsPbBr_3$ Gamma-Ray Detectors. *ACS Appl. Mater. Interfaces* **2023**, *15*, 16895−16901.
(33) Sun, Q.; Ge, B.; Xiao, B.; Li, F.; Ji, L.; Yin, Z.; Guo, J.; Tang, J.; Zhou, C.; Jie, W.; Zhu, M.; Xu, Y. High-Performance Industrial-Grade $CsPbBr_3$ Single Crystal by Solid-Liquid Interface Engineering. *Adv. Sci.* **2023**, *10*, 2302236.
(34) Pan, L.; He, Y.; Klepov, V. V.; De Siena, M. C.; Kanatzidis, M. G. Perovskite $CsPbBr_3$ Single Crystal Detector for High Flux X-Ray Photon Counting. *IEEE Trans. Med. Imag.* **2022**, *41*, 3053−3061.

https://doi.org/10.1021/acsami.4c00432
ACS Appl. Mater. Interfaces 2024, 16, 12106−12114

(35) He, Y.; Stoumpos, C. C.; Hadar, I.; Luo, Z.; McCall, K. M.; Liu, Z.; Chung, D. Y.; Wessels, B. W.; Kanatzidis, M. G. Demonstration of Energy-Resolved Gamma-Ray Detection at Room Temperature by the $CsPbCl_3$ Perovskite Semiconductor. *J. Am. Chem. Soc.* **2021**, *143*, 2068−2077.
(36) He, Y.; Hadar, I.; Kanatzidis, M. G. Detecting Ionizing Radiation using Halide Perovskite Semiconductors Processed through Solution and Alternative methods. *Nat. Photonics* **2022**, *16*, 14−26.
(37) He, Y.; Petryk, M.; Liu, Z.; Chica, D. G.; Hadar, I.; Leak, C.; Ke, W.; Spanopoulos, I.; Lin, W.; Chung, D. Y.; Wessels, B. W.; He, Z.; Kanatzidis, M. G. $CsPbBr_3$ Perovskite Detectors with 1.4% Energy Resolution for High-Energy γ-Rays. *Nat. Photonics* **2021**, *15*, 36−42.
(38) He, Y.; Matei, L.; Jung, H. J.; McCall, K. M.; Chen, M.; Stoumpos, C. C.; Liu, Z.; Peters, J. A.; Chung, D. Y.; Wessels, B. W.; Wasielewski, M. R.; Dravid, V. P.; Burger, A.; Kanatzidis, M. G. High Spectral Resolution of Gamma-Rays at Room Temperature by Perovskite $CsPbBr_3$ Single Crystals. *Nat. Commun.* **2018**, *9*, 1609.
(39) He, Y.; Ke, W.; Alexander, G. C. B.; McCall, K. M.; Chica, D. G.; Liu, Z.; Hadar, I.; Stoumpos, C. C.; Wessels, B. W.; Kanatzidis, M. G. Resolving the Energy of γ-Ray Photons with $MAPbI_3$ Single Crystals. *ACS Photonics* **2018**, *5*, 4132−4138.
(40) Ulatowski, A. M.; Wright, A. D.; Wenger, B.; Buizza, L. R. V.; Motti, S. G.; Eggimann, H. J.; Savill, K. J.; Borchert, J.; Snaith, H. J.; Johnston, M. B.; Herz, L. M. Charge-Carrier Trapping Dynamics in Bismuth-Doped Thin Films of $MAPbBr_3$ Perovskite. *J. Phys. Chem. Lett.* **2020**, *11*, 3681−3688.
(41) Meng, R.; Wu, G.; Zhou, J.; Zhou, H.; Fang, H.; Loi, M. A.; Zhang, Y. Understanding the Impact of Bismuth Heterovalent Doping on the Structural and Photophysical Properties of CH_3 NH_3 $PbBr_3$ Halide Perovskite Crystals with Near-IR Photoluminescence. *Chemistry* **2019**, *25*, 5480−5488.
(42) Mosconi, E.; Merabet, B.; Meggiolaro, D.; Zaoui, A.; De Angelis, F. First-Principles Modeling of Bismuth Doping in the $MAPbI_3$ Perovskite. *J. Phys. Chem. C* **2018**, *122*, 14107−14112.
(43) Yang, F.; Zhang, H.; Li, L.; Reaney, I. M.; Sinclair, D. C. High Ionic Conductivity with Low Degradation in A-Site Strontium-Doped Nonstoichiometric Sodium Bismuth Titanate Perovskite. *Chem. Mater.* **2016**, *28*, 5269−5273.
(44) Pan, D.; Fu, Y.; Chen, J.; Czech, K. J.; Wright, J. C.; Jin, S. Visualization and Studies of Ion-Diffusion Kinetics in Cesium Lead Bromide Perovskite Nanowires. *Nano Lett.* **2018**, *18*, 1807−1813.
(45) Clark, J. N.; Ihli, J.; Schenk, A. S.; Kim, Y. Y.; Kulak, A. N.; Campbell, J. M.; Nisbet, G.; Meldrum, F. C.; Robinson, I. K. Three-Dimensional Imaging of Dislocation Propagation During Crystal Growth and Dissolution. *Nat. Mater.* **2015**, *14*, 780−784.

https://doi.org/10.1021/acsami.4c00432
ACS Appl. Mater. Interfaces 2024, 16, 12106−12114